

Trions in cylindrical nanowires with a dielectric mismatch

A. F. Slachmuylders,^{1,*} B. Partoens,^{1,†} W. Magnus,^{1,2,‡} and F. M. Peeters^{1,§}

¹*Departement Fysica, Universiteit Antwerpen, Groenenborgerlaan 171, B-2020 Antwerpen, Belgium*

²*Interuniversity Microelectronics Centre, Kapeldreef 75, B-3001 Leuven, Belgium*

(Received 16 March 2007; published 6 August 2007)

We investigated the lowest energy levels of trions (charged excitons) in freestanding nanowires with strong lateral carrier confinement. Within the adiabatic approximation, the three-particle problem reduces to an effective two-dimensional Schrödinger equation for the relative motion which is solved numerically. Dielectric mismatch effects are taken into account, which results in a distorted Coulomb interaction between the charged particles. We obtain the “bright” singlet and triplet trion binding energies and we found that the negatively charged exciton is always less stable than the positively charged exciton in a wire with a hole to electron mass ratio $\sigma > 1$. The pair correlation functions and the conditional probabilities are calculated, which visualizes the correlation between the particles in the wire.

DOI: [10.1103/PhysRevB.76.075405](https://doi.org/10.1103/PhysRevB.76.075405)

PACS number(s): 73.21.Hb, 78.67.Lt

I. INTRODUCTION

When an additional electron or hole is bound to an exciton (X), a charged exciton or *trion* (X^+ or X^-) is formed. Their existence in bulk semiconductors was first predicted theoretically in the 1950s by Lampert,¹ but due to the low binding energies, they could only be observed in bulk materials at very low temperatures,^{2,3} restricting the practical relevance of these many-particle systems. However, trions become of importance when the dimensionality is reduced: confinement results in enhanced binding energies^{4,5} and consequently these complexes become observable at higher temperatures.

Due to recent progress in semiconductor nanowire growth, it became possible to grow nanowires with small diameters and large aspect ratio.⁶ Tremendous effort has been devoted to nanowire growth, motivated by their unique electronic and optical properties and their potential use in novel electronic⁷⁻⁹ and photonic^{10,11} devices.

Stability of negative and positive trions has been investigated previously in quantum wires,¹² rods,¹³ wells,¹⁴ and dots¹⁵ but, to our knowledge, nobody has investigated trions in wires in the presence of a dielectric mismatch, which is the goal of our paper. When the Coulomb interaction is small as compared to the radial confinement, the adiabatic approximation can be used, which reduces the dimension of the problem from nine to two. Within the framework of the effective mass approximation, the reduced Schrödinger equation will be solved numerically using the finite element technique that enables us to calculate the trion binding energies for a whole range of wire materials and wire surroundings. Extending our previous work on quantum wire excitons,¹⁶ we will calculate positive and negative trion binding energies as function of hole and electron mass ratio, dielectric constants, and wire radius. Also, the trion wave function will be investigated.

The paper is organized as follows. In Sec. I, we focus on the theoretical calculation and present the effective trion Hamiltonian. In Sec. II, we construct the trion potential, with the aid of our previously obtained results on excitons. The calculations of the trion binding energy and wave function

are presented in Sec. III. Finally, we summarize our main results in Sec. IV.

II. EFFECTIVE HAMILTONIAN

The trion Hamiltonian in the effective mass approximation is given by

$$H_{\pm} = \sum_i \left(-\frac{\hbar^2}{2m_i} \nabla_i^2 + V_i(\vec{r}_i) \right) + \sum_{i<j} W(\vec{r}_i - \vec{r}_j), \quad (1)$$

where the index $i=e_1, e_2, h$ for X^- , while $i=h_1, h_2, e$ for X^+ , e_i (h_i) refers to electron (hole), and $V_i(\vec{r}_i)$ is the particle confinement potential. $W(\vec{r}_i - \vec{r}_j)$ is the electrostatic potential energy due to interparticle interaction, which will be discussed later.

From now on, we focus on the calculations for X^- as the results for X^+ can be obtained in a similar way. We assume that the lateral confinement is sufficiently large to decouple the lateral and transverse motion. With this assumption, the trion wave function can be separated into a product

$$\Psi(\vec{r}_{e_1}, \vec{r}_{e_2}, \vec{r}_h) = \psi_e(x_{e_1}, y_{e_1}) \psi_e(x_{e_2}, y_{e_2}) \psi_h(x_h, y_h) \chi_{-}(z_{e_1}, z_{e_2}, z_h). \quad (2)$$

This amounts to adopting the adiabatic approximation, thereby taking the single-particle states for a cylindrical quantum wire $\psi_{e(h)}(x, y)$ as the lateral particle wave functions. This is justified as long as the Coulomb energy is much weaker than the single-particle confinement energy. In freestanding quantum wires, the confinement potential $V_{e(h)}$ is a circular quantum well. The barrier height is determined by the electron affinity and is approximated by infinity. The single-particle states in such a well are Bessel functions $J_l(x)$. Taking the expectation value of Eq. (1) with the single-particle wave functions of Eq. (2), the simplified Hamiltonian reads

$$H_{-} = H_{e_1} + H_{e_2} + H_h + H_{-}^{\text{eff}}, \quad (3)$$

where $H_{e_1, e_2, h}$ are the Hamiltonians of the noninteracting particles and

$$H_-^{\text{eff}} = -\frac{\hbar^2}{2m_e} \left[\frac{\partial^2}{\partial z_{e_1}^2} + \frac{\partial^2}{\partial z_{e_2}^2} \right] - \frac{\hbar^2}{2m_h} \frac{\partial^2}{\partial z_h^2} + U_{\text{tot}}(z_{e_1}, z_{e_2}, z_h), \quad (4)$$

with

$$U_{\text{tot}}(z_{e_1}, z_{e_2}, z_h) = \int_{\text{wire}} dx_{e_1} dy_{e_1} dx_{e_2} dy_{e_2} dx_h dy_h [W(\vec{r}_{e_1} - \vec{r}_h) + W(\vec{r}_{e_2} - \vec{r}_h) + W(\vec{r}_{e_1} - \vec{r}_{e_2})] \times |\psi_e(x_{e_1}, y_{e_1})|^2 |\psi_e(x_{e_2}, y_{e_2})|^2 |\psi_h(x_h, y_h)|^2. \quad (5)$$

Finally, we reduce the effective Hamiltonian by introducing the center-of-mass coordinate Z and the relative electron-hole positions z_{h1} and z_{h2} ,

$$Z = \frac{z_{e_1} + z_{e_2} + \sigma z_h}{2 + \sigma}, \quad (6)$$

$$z_{h1} = z_h - z_{e_1}, \quad (7)$$

$$z_{h2} = z_h - z_{e_2}, \quad (8)$$

yielding

$$H_-^{\text{eff}} = -\frac{\hbar^2}{m_e} \frac{1}{2M} \frac{\partial^2}{\partial Z^2} + H_-^{\text{rel}}, \quad (9)$$

where $M=2+\sigma$ is the X^- trion mass and $\sigma=m_h/m_e$ the hole to electron mass ratio. With $\mu=\sigma/(1+\sigma)$ the reduced mass of an electron-hole pair, we can write

$$H_-^{\text{rel}} = \frac{\hbar^2}{m_e} \left[-\frac{1}{2\mu} \left(\frac{\partial^2}{\partial z_{h1}^2} + \frac{\partial^2}{\partial z_{h2}^2} \right) - \frac{1}{\sigma} \frac{\partial^2}{\partial z_{h1} \partial z_{h2}} \right] + U_{\text{tot}}(z_{h1}, z_{h2}), \quad (10)$$

which allows us to separate the wave function χ_- into a product of the center of mass and relative wave functions, i.e., $\chi_- = \chi_{\text{c.m.}}(Z)\chi(z_{h1}, z_{h2})$, and to reduce the original problem to the solution of a two-dimensional (2D) Schrödinger equation.

Analogously, a positive trion X^+ may be represented by

$$H_+^{\text{rel}} = \frac{\hbar^2}{m_e} \left[-\frac{1}{2\mu} \left(\frac{\partial^2}{\partial z_{h1}^2} + \frac{\partial^2}{\partial z_{h2}^2} \right) - \frac{\partial^2}{\partial z_{h1} \partial z_{h2}} \right] + U_{\text{tot}}(z_{h1}, z_{h2}), \quad (11)$$

where z_{h1} and z_{h2} denote the relative position coordinates of the first and the second hole with respect to the electron position.

III. EFFECTIVE 2D TRION POTENTIAL

In order to calculate the effective 2D potential U_{tot} mentioned in Eq. (10), we need an explicit expression for $W_{\text{tot}} = W(\vec{r}_{e_1} - \vec{r}_h) + W(\vec{r}_{e_2} - \vec{r}_h) + W(\vec{r}_{e_1} - \vec{r}_{e_2})$. For that purpose, we express W_{tot} in terms of the electrostatic potential V_{in} , the potential inside a wire at a point $\vec{r}=(\rho, \theta, z)$ due to a charge e at $\vec{r}'=(\rho', \theta', z')$,

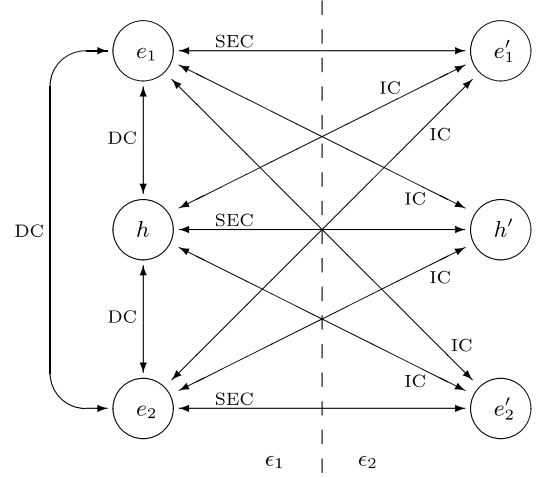


FIG. 1. Schematic drawing of electrons (e_1 and e_2) and hole (h) near an interface with the indication of the different interactions between the electrons and hole and their images e'_1 , e'_2 , and h' .

$$W_{\text{tot}} = \frac{1}{2} \int d\vec{r} [e \delta(\vec{r} - \vec{r}_{e_1}) + e \delta(\vec{r} - \vec{r}_{e_2}) - e \delta(\vec{r} - \vec{r}_h)] \times [V_{\text{in}}(\vec{r}, \vec{r}_{e_1}) + V_{\text{in}}(\vec{r}, \vec{r}_{e_2}) - V_{\text{in}}(\vec{r}, \vec{r}_h)]. \quad (12)$$

An expression for $V_{\text{in}}(\vec{r}, \vec{r}')$ can be obtained by solving the appropriate Poisson equation and is given by (see Ref. 16 for details)

$$V_{\text{in}}(\vec{r}, \vec{r}') = \frac{e}{4\pi\epsilon_1} \left[\frac{1}{|\vec{r} - \vec{r}'|} + \frac{2}{\pi} \left(\frac{\epsilon_1}{\epsilon_2} - 1 \right) \times \sum_{m=-\infty}^{+\infty} e^{im(\theta-\theta')} \int_0^{\infty} dk \cos(k(z-z')) \right] \times C_m \left(kR, \frac{\epsilon_1}{\epsilon_2} \right) I_m(k\rho) I_m(k\rho'), \quad (13)$$

where ϵ_1/ϵ_2 is the ratio of dielectric constants inside and outside the wire and

$$C_m \left(kR, \frac{\epsilon_1}{\epsilon_2} \right) = \frac{K_m(kR) K'_m(kR)}{I_m(kR) K'_m(kR) - \frac{\epsilon_1}{\epsilon_2} I'_m(kR) K_m(kR)}. \quad (14)$$

Following Ref. 17, we subtract the electrostatic self-energy coming from the terms proportional to

$$\frac{\delta(\vec{r} - \vec{r}_{e_1})}{|\vec{r} - \vec{r}_{e_1}|} + \frac{\delta(\vec{r} - \vec{r}_{e_2})}{|\vec{r} - \vec{r}_{e_2}|} + \frac{\delta(\vec{r} - \vec{r}_h)}{|\vec{r} - \vec{r}_h|} \quad (15)$$

in the integral of Eq. (12), yielding the total interaction energy

$$\delta W = W_{\text{dir}} + W_{\text{ind}} + W_{\text{ind,S}}, \quad (16)$$

where

$$W_{\text{ind,S}}(\vec{r}_{e_1}, \vec{r}_{e_2}, \vec{r}_h) = \frac{e^2}{4\pi^2\epsilon_1} \left(\frac{\epsilon_1}{\epsilon_2} - 1 \right) \sum_{m=-\infty}^{+\infty} \int_0^\infty dk C_m \left(kR, \frac{\epsilon_1}{\epsilon_2} \right) [I_m^2(k\rho_{e_1}) + I_m^2(k\rho_{e_2}) + I_m^2(k\rho_h)], \quad (18)$$

$$W_{\text{ind}}(\vec{r}_{e_1}, \vec{r}_{e_2}, \vec{r}_h) = -2 \frac{e^2}{4\pi^2\epsilon_1} \left(\frac{\epsilon_1}{\epsilon_2} - 1 \right) \sum_{m=-\infty}^{+\infty} \int_0^\infty dk C_m \left(kR, \frac{\epsilon_1}{\epsilon_2} \right) [\cos(kz_{h1})\cos(m(\theta_{e_1} - \theta_h))I_m(k\rho_{e_1})I_m(k\rho_h) \\ + \cos(kz_{h2})\cos(m(\theta_{e_2} - \theta_h))I_m(k\rho_{e_2})I_m(k\rho_h) - \cos(k(z_{e_1} - z_{e_2}))\cos(m(\theta_{e_1} - \theta_{e_2}))I_m(k\rho_{e_1})I_m(k\rho_{e_2})] \quad (19)$$

are the modifications of this interaction due to the image charges induced by the difference in permittivity between the wire and its surrounding environment.

These expressions clearly show the different contributions to the electrostatic energy δW as illustrated by the labeled arrows in Fig. 1:

(1) three direct contributions (DC) of the regular Coulomb potential in W_{dir} [Eq. (17)] representing the Coulomb interaction between each of the particles,

(2) three self-energy contributions (SEC) $W_{\text{ind,S}}$ emerging from the interaction between an induced image charge and the original charge (that produces the image), and

(3) induced contributions (IC) W_{ind} emerging from the interaction between a charge in the wire and an induced image charge produced by another charge.

The next step is to average the contributions W_{dir} , $W_{\text{ind,S}}$, and W_{ind} with the single-particle radial wave functions in order to obtain the effective potential energies, respectively, U_{dir} , E_{self} , and U_{ind} . In previous work,^{16,18} we obtained the following fits for the three contributions: the direct potential energy is given by

$$\tilde{U}_{\text{dir}}(z) = \frac{\gamma|z| + \delta}{z^2 + \eta|z| + \beta}, \quad (20)$$

with $\gamma=-1$, $\delta=-1.22$, $\eta=1.13$, and $\beta=0.47$ for the electron and hole in the ground state. The induced potential was found to be

$$\tilde{U}_{\text{ind}}(z) = \frac{p|z| + \tilde{U}_{\text{ind}}(z=0)s}{z^2 + r|z| + s}, \quad (21)$$

where the parameters depend on the dielectric constants inside and outside the wire and are given by

$$p = 0.86[1 - (\epsilon_1/\epsilon_2)^{1.05}], \quad (22a)$$

$$r = 0.84 + 0.23(\epsilon_1/\epsilon_2)^{3/4}, \quad (22b)$$

$$W_{\text{dir}}(\vec{r}_{e_1}, \vec{r}_{e_2}, \vec{r}_h) = \frac{e^2}{4\pi\epsilon_1} \left(\frac{1}{|\vec{r}_{e_1} - \vec{r}_{e_2}|} - \frac{1}{|\vec{r}_{e_1} - \vec{r}_h|} - \frac{1}{|\vec{r}_{e_2} - \vec{r}_h|} \right) \quad (17)$$

is the direct Coulomb interaction in the absence of a dielectric mismatch and

$$s = 1.57 + 1.02(\epsilon_1/\epsilon_2), \quad (22c)$$

$$\tilde{U}_{\text{ind}}(z=0) = 1.36[1 - (\epsilon_1/\epsilon_2)^{2/3}]. \quad (22d)$$

Please note that in these expressions, all interparticle distances z are in units of the wire radius R . Also note that $\tilde{U}_{\text{dir}} = U_{\text{dir}}/E_0$, $\tilde{U}_{\text{ind}} = U_{\text{ind}}/E_0$, and $E_0 = e^2/4\pi\epsilon_1 R$. Finally, for the self-energy we found the following fit:

$$\frac{E_{\text{self}}}{E'_0} = \frac{a[(\epsilon_1/\epsilon_2)^b - 1]}{\epsilon_1/\epsilon_2}, \quad (23)$$

with $a=0.89$, $b=0.59$, and $E'_0 = e^2/4\pi\epsilon_2 R$. Reusing these analytic expressions, we are able to construct the 2D effective trion potential:

$$U_{\text{tot}} = \tilde{U}_{\text{dir}}(z_{h1} - z_{h2}) + \tilde{U}_{\text{dir}}(z_{h1}) + \tilde{U}_{\text{dir}}(z_{h2}) + \tilde{U}_{\text{ind}}(z_{h1} - z_{h2}) \\ + \tilde{U}_{\text{ind}}(z_{h1}) + \tilde{U}_{\text{ind}}(z_{h2}) + 3 \frac{E_{\text{self}}}{E'_0}. \quad (24)$$

Three-dimensional and contour plots of the sum of direct and induced potentials for four different values of the dielectric mismatch are shown in Fig. 2. In this figure, we did not include the constant self-energy which is independent of z_{h1} and z_{h2} , since this merely results in an increase of the band gap without affecting the trion binding energy. In Fig. 2, we see that the potential exhibits a maximum for $z_{h1} = z_{h2}$, which corresponds to the configuration $z_{e_1} = z_{e_2}$ (for X^-) for which a strong repulsion between the two electrons is apparent. Lines of minima (attraction) are present in the potential energy for $z_{e_1} = z_h$ (i.e., $z_{h1} = 0$) and $z_{e_2} = z_h$ (i.e., $z_{h2} = 0$). As the dielectric mismatch is increased, the potential becomes slightly deformed: the larger the dielectric mismatch, the more pronounced are the minima and maxima.

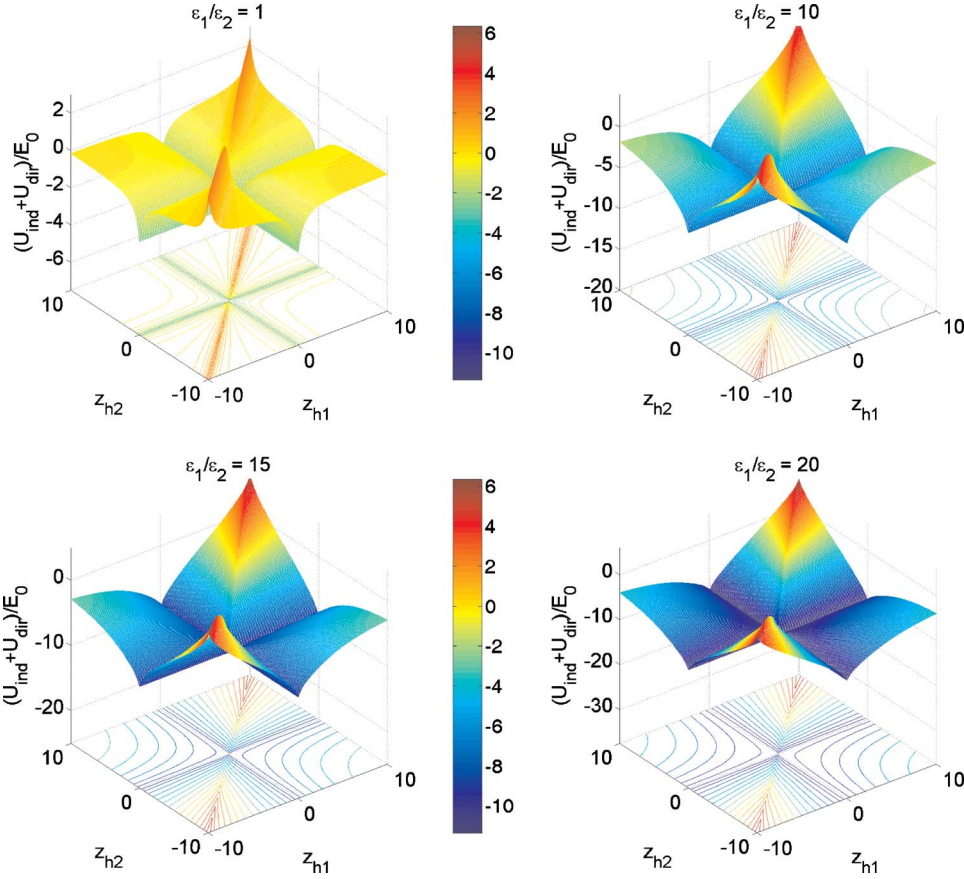


FIG. 2. (Color online) Three-dimensional and contour plots of the sum of induced and direct interaction potentials for $\epsilon_1/\epsilon_2=1, 10, 15,$ and 20 . Note that the potential is plotted in units of $E_0=e^2/4\pi\epsilon_1R$.

IV. TRION BINDING ENERGY AND WAVE FUNCTION

Next, we insert the effective 2D trion potential into the Schrödinger equation [Eq. (10)] and solve the latter on a 2D grid and obtain wave functions and energies. Introducing the wire radius R as the unit of length and setting $a_{b,0}=4\pi\epsilon_0\hbar^2/(m_e e^2)$, $E_0''=e^2/(4\pi\epsilon_0 a_{b,0})$, and $E_0=e^2/(4\pi\epsilon_1 R)$, we can rewrite Eq. (10) in a dimensionless form,

$$H_-^{\text{rel}} = \left(\frac{a_{b,0}}{R}\right)^2 \left[-\frac{1}{2\mu} \left(\frac{\partial^2}{\partial z_{h1}^2} + \frac{\partial^2}{\partial z_{h2}^2} \right) - \frac{1}{\sigma} \frac{\partial^2}{\partial z_{h1} \partial z_{h2}} \right] + \left(\frac{a_{b,0}}{R}\right) \frac{\epsilon_2}{\epsilon_1} \frac{U_{\text{tot}}}{E_0}, \quad (25)$$

where we set $\epsilon_2/\epsilon_0=1$. Similarly, we obtain for the positive trion the following Hamiltonian for the relative motion:

$$H_+^{\text{rel}} = \left(\frac{a_{b,0}}{R}\right)^2 \left[-\frac{1}{2\mu} \left(\frac{\partial^2}{\partial z_{h1}^2} + \frac{\partial^2}{\partial z_{h2}^2} \right) - \frac{\partial^2}{\partial z_{h1} \partial z_{h2}} \right] + \left(\frac{a_{b,0}}{R}\right) \frac{\epsilon_2}{\epsilon_1} \frac{U_{\text{tot}}}{E_0}. \quad (26)$$

The reference energies in both cases are the single-particle energies, i.e., $E_{e_1}+E_{e_2}+E_h$ for X^- and $E_{h_1}+E_{h_2}+E_e$ for X^+ . Therefore, the lowest energy eigenvalues of Eqs. (25) and (26) correspond to the energy to break up the trion in three separate particles moving freely along the wire.

However, our main interest is to determine the binding energy of the trion, i.e., the energy needed to break up the trion into an exciton and one free particle:

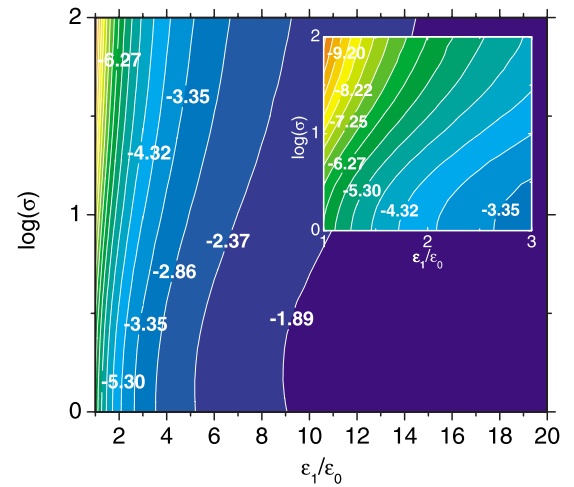


FIG. 3. (Color online) Contour plot of the X^+ ground state binding energy in units of $E_0''/1000=[e^2/(4\pi\epsilon_0 a_{b,0})] \times [1/1000]$ as a function of the dielectric constant of the wire (with $\epsilon_2/\epsilon_0=1$) and the electron-hole mass ratio σ . The inset figure shows the same as the main figure, but now zoomed in to the region $1 \leq \epsilon_1/\epsilon_0 \leq 3$. The result is shown for $R/a_{b,0}=20$.

TABLE I. Table with relevant material parameters for freestanding nanowires. For silicon, we mentioned the transverse (t) and lateral (l) mass at the X point, as well as the mass in the Γ point. The value of $R/a_{b,0}$ in the last column was calculated for $R=10$ nm.

	m_e (m_0)	m_{hh} (m_0)	ϵ_1 (ϵ_0)	$a_{b,0}$ (nm)	E_0'' (eV)	σ	R ($a_{b,0}$)
Si at X (t)	0.1905	0.49	11.9	0.28	5.17	2.58	35.8
Si at X (l)	0.9163	0.49	11.9	0.06	24.86	0.53	172.7
Si at Γ	0.20	0.49	11.9	0.27	5.43	2.45	37.7
InP	0.0798	0.53	12.4	0.66	2.16	6.64	15.0
ZnO	0.24	0.78	8.1	0.22	6.51	3.25	45.2
Ge	0.082	0.28	16	0.65	2.22	3.41	15.5
GaAs	0.067	0.35	12.5	0.79	1.82	5.22	12.6
InAs	0.026	0.33	14.6	2.04	0.71	12.69	4.9

$$E_B(X^\pm) = E(X^\pm) - E(X). \quad (27)$$

Please note that both $E(X^\pm)$ and $E(X)$ are the many-particle energies as referred to the single-particle energy of their constituents. The exciton binding energy was obtained previously in Ref. 16. In Table I, material parameters are given for a few materials.^{19–21}

Contour plots of the binding energy for freestanding wires ($\epsilon_2/\epsilon_0=1$) as a function of the dielectric constant of the wire ϵ_1/ϵ_0 for different values of σ are shown in Figs. 3 and 4 for the positive trion X^+ , where the binding energy values indicated at the contour lines are given in units of $E_0''/1000 = [e^2/(4\pi\epsilon_0 a_{b,0})] \times [1/1000]$. The energy of the ground state (Fig. 3) and the first excited state (Fig. 4) has been calculated. We can see that for a small fixed value of ϵ_1/ϵ_0 , the ground state binding energy varies more rapidly with σ than for a large fixed value of ϵ_1/ϵ_0 . The picture for the first excited state is slightly different, but again most changes in the binding energy occur in the region of small dielectric constants.

For the negative and less stable trion X^- , we only calculated the ground state binding energy in Fig. 5. The funda-

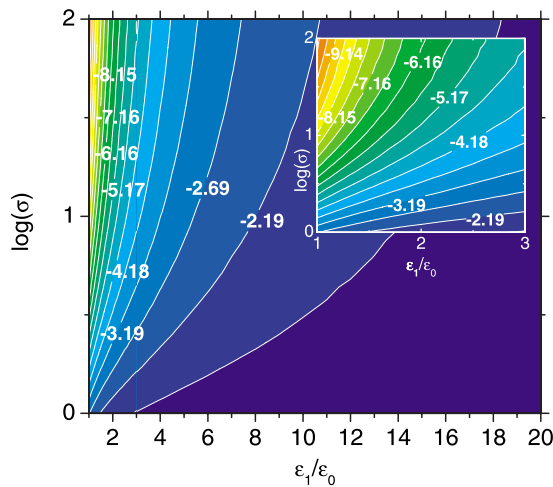


FIG. 4. (Color online) The same as Fig. 3 but now for the X^+ first excited state binding energy.

mental difference with the positively charged trion is that now the contour lines are essentially parallel, which means that the X^- binding energy is only weakly dependent on σ . As the dielectric constant ϵ_1/ϵ_0 is increased, the contour lines become slightly more bent, but the overall conclusion is clear: the parameter σ almost does not affect the X^- binding energy.

In Figs. 6, 7, and 9 we show the wave functions for X^+ and X^- for various values of σ and ϵ_1/ϵ_0 . In Fig. 6, we see the ground state wave function for the X^+ trion. It is clear that increasing σ mainly changes the shape of the wave function: the maxima are pulled further away from each other and a node along the $z_{h1}=z_{h2}$ is created, and the particles also become more localized. With increasing ϵ_1/ϵ_0 , the extent of the wave function is changing (i.e., it increases with increasing ϵ_1/ϵ_0), while its shape is practically unaltered. With increasing σ (i.e., increasing hole mass), the exciton wave function becomes more localized and the wave function condenses into two well-separated pockets. In Fig. 7, the excited state wave function of X^+ is plotted. It is clear that for $\sigma=10$, the wave functions for the ground state and the excited state will result in a similar probability function and thus they result in (almost) degenerate values of the energy. For

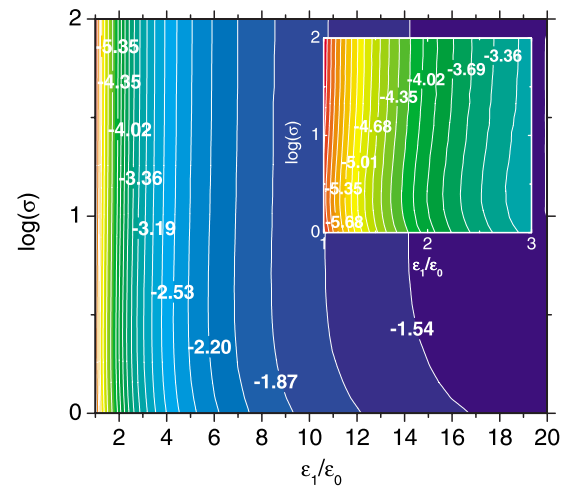


FIG. 5. (Color online) The same as Fig. 3 but now for the X^- ground state binding energy.

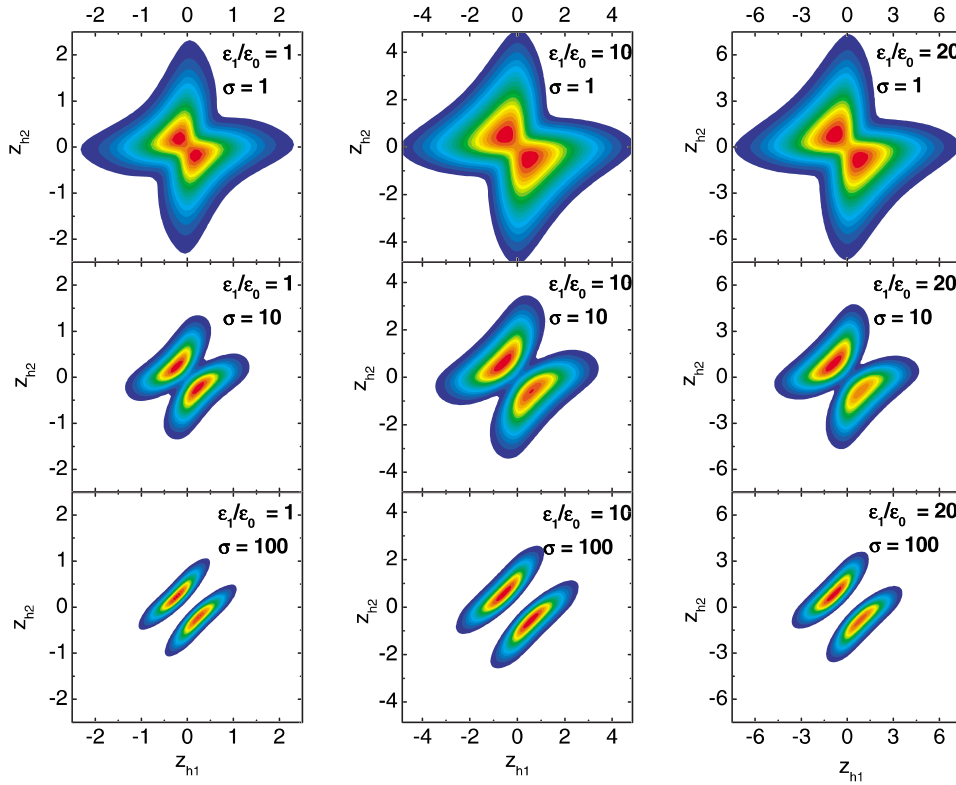


FIG. 6. (Color online) Plots of the X^+ ground state wave function for several values of σ and ϵ_1/ϵ_0 . The result is shown for $R/a_{b,0} = 20$.

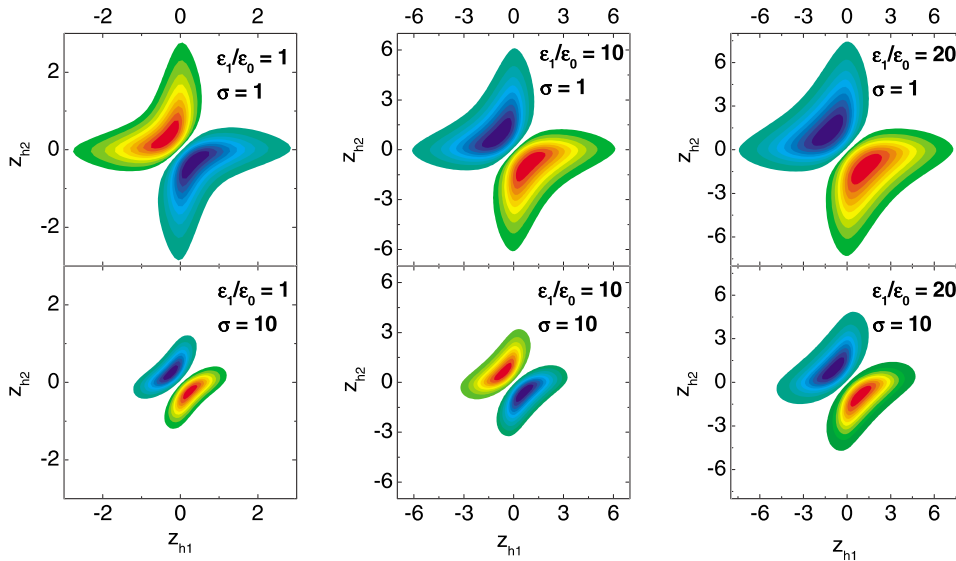


FIG. 7. (Color online) Plots of the X^+ first excited state wave function for several values of σ and ϵ_1/ϵ_0 . For larger values of σ , the wave function of the excited state will result in the same probability density as for the ground state: degeneracy sets in. The only difference is that for the excited state, the wave functions are antisymmetric with respect to the interchange of holes, whereas for the ground state, they are symmetric. The result is shown for $R/a_{b,0} = 20$.

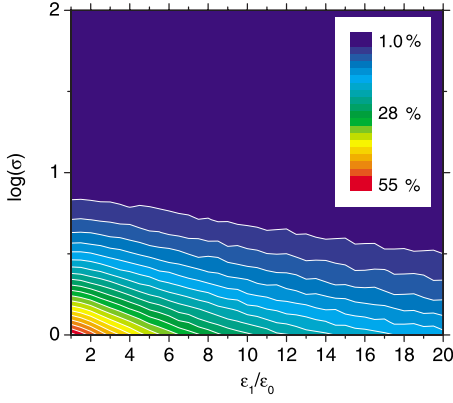


FIG. 8. (Color online) Plot of the percentual energy difference between the ground and excited states for the X^+ trion. The darkest blue zone represents the area where the energy is practically degenerate.

larger values of σ ($\sigma \geq 10$), the ground state and excited state become degenerate for X^+ . Figure 8 shows the percentual energy difference between both ground and excited states and the darkest blue zone represents the area where the difference is (almost) zero. Figure 9 shows several contour plots of the X^- wave function. Notice again how a change in ϵ_1/ϵ_0 modifies the size of the wave function. As was to be expected from the energy contour plots, the wave function does not change significantly when σ is increased.

When increasing σ , the maxima come closer together for the X^- trion, whereas for the X^+ trion the maxima are pulled further apart from each other: for the electrons in the X^- trion it becomes more easy to tunnel through the barrier along the $z_{h1}=z_{h2}$ diagonal of the potential with increasing σ , but for the heavier holes this becomes more and more difficult as σ increases.

The correlation between particles within the X^\pm trions is reflected even more clearly in the pair correlation functions. The correlation functions can be expressed through

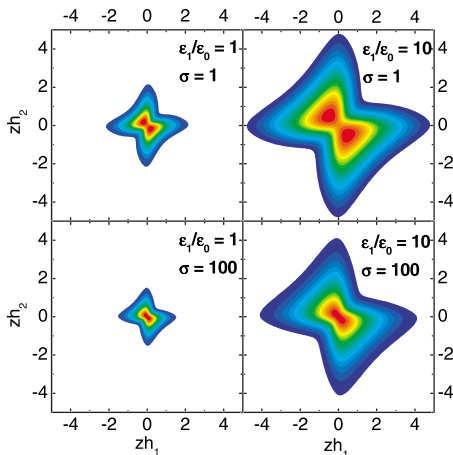


FIG. 9. (Color online) Plots of the ground state wave function for several values of σ and ϵ_1/ϵ_0 for X^- . The result is again shown for $R/a_{b,0}=20$.

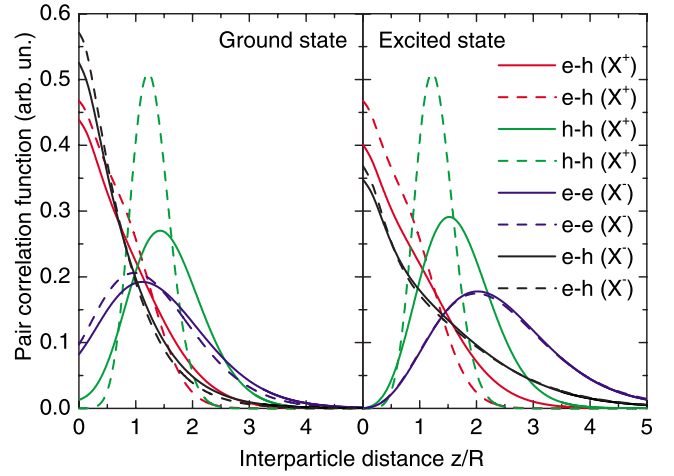


FIG. 10. (Color online) Ground state (left) and excited state (right) X^+ and X^- pair correlation functions for electron-electron, hole-hole and electron-hole interactions for $\sigma=5$ (full lines) and $\sigma=50$ (dashed lines). The calculation was done for $R/a_{b,0}=20$ and $\epsilon_1/\epsilon_0=10$.

$$f_{eh}(z) = \int \int dz_{h1} dz_{h2} |\chi(z_{h1}, z_{h2})|^2 \delta(z - z_{h1}) \quad (28)$$

for the electron-hole correlation and

$$f_{eelhh}(z) = \int \int dz_{h1} dz_{h2} |\chi(z_{h1}, z_{h2})|^2 \delta(z - (z_{h1} - z_{h2})) \quad (29)$$

for the electron-electron or hole-hole correlation. The results are shown in Fig. 10. Notice that for the ground state, (i) the light electrons can still tunnel through the potential barrier for zero interparticle distance, whereas this is more difficult for the heavier holes, (ii) increasing σ has the opposite effect on the positive and negative trions at zero interparticle distance, and (iii) the electron-hole correlation is the largest at

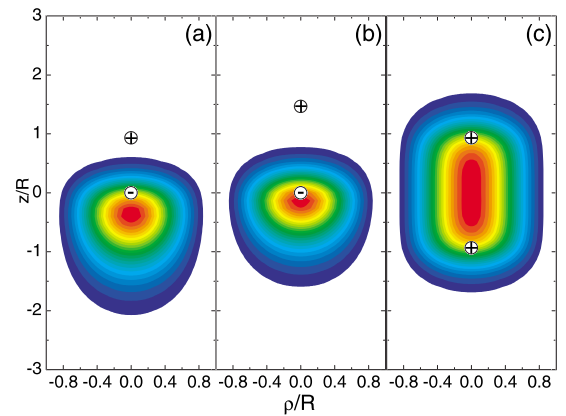


FIG. 11. (Color online) [(a) and (b)] X^+ conditional probability plots for an electron fixed at $z/R=0$ and one of the holes fixed at two different positions. (c) Both holes are fixed. The highest probability of finding the remaining particle corresponds to the red areas. These plots were made for $R/a_{b,0}=20$, $\epsilon_1/\epsilon_0=10$, and $\sigma=5$.

zero interparticle distance, i.e., oppositely charged particles prefer to sit on top of each other. For the excited state correlation function, we find that (i) the e - e and h - h correlation functions are exactly zero for zero interparticle distance for both trions because of the asymmetry of the wave function at $z/R=0$ and (ii) the e - h correlation for the X^+ is larger than for the X^- (it was vice versa in the ground state): both particles are more bound to each other for the X^+ excited state than for the X^- excited state. From Figs. 6 and 9, we can also conclude that the ground state wave functions for both trions are symmetric with respect to the interchange of holes or electrons. This means that since the system consists of fermions, the spin part of the total wave function must be antisymmetric and therefore the ground state wave functions are singlet states. The excited state wave functions, however, are antisymmetric and thus correspond to triplet states in this case. From Ref. 22, we find that the trion singlet state consists of two different spin states, whereas the trion triplet consists of six different spin states. In the presence of a magnetic field, the degeneracy of these states is lifted. Here, the trion spin states are constructed by taking the orbital angular momentum for transverse motion $l=0$ for all particles and are consequently “bright” triplets. Triplet states with lower energy but with angular momentum different from zero may exist for thick wires. However, as these triplet states are “dark” states, thus optically inactive, we did not consider those states here.

Furthermore, we also plotted the conditional probability as a function of several electron and hole positions for X^\pm . This probability is given by $|\Psi|^2$ where two particles out of the three are fixed in space. In Fig. 11(a), we placed for the X^+ trion an electron in the origin and a hole at a distance which corresponds to the average electron-hole distance in the X^+ . Note that the hole is most likely to be found near the electron, i.e., it is drawn to the electron but on the other hand it is also repelled by the hole. When the electron-hole distance increases [Fig. 11(b)], the hole is able to get closer to the electron. In 11(c), it is clear that the electron can be found, with equal probability, in the vicinity of one of the holes: the probability function is symmetric with respect to the origin. Figures 12(a)–12(c) show similar pictures for the X^- as for the X^+ trion. Notice that the electron cloud is much more spread out as a consequence of the lighter mass of the electron. Similarly, the hole cloud is more concentrated between the two electrons.

In Table I, it is clear that our main focus is on the $1 \leq \sigma \leq 10$ interval and therefore we plotted in Fig. 13 the singlet and triplet binding energies for this interval for $\epsilon_1/\epsilon_0=5, 10,$ and 15 and $R/a_{b,0}=20$. As it should be, the binding energies are identical for both positive and negative trions when $\sigma=1$. When σ increases, we see that (i) the ground state binding energy for the X^- trion is quasiconstant and the ground state for the X^+ trion becomes clearly more stable for all values of ϵ_1/ϵ_0 ; (ii) the binding energy of the first excited state of X^- decreases with increasing σ , whereas its ground state energy stays quasiconstant; and (iii) the first excited state of the X^+ comes close to degeneracy with its ground state and becomes more stable than the X^- ground state for σ between 3 and 4.

Finally, we calculated the singlet and triplet X^+ and X^- trion binding energies as function of the radius $R/a_{b,0}$. This

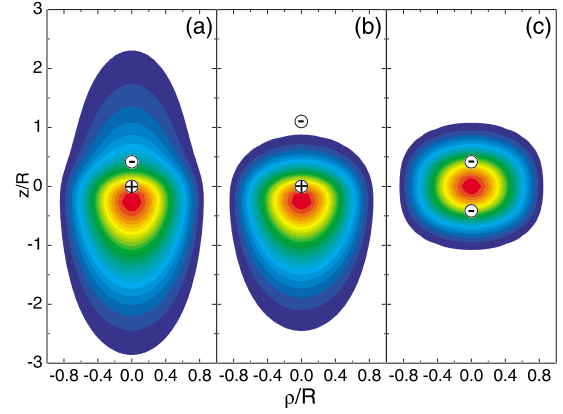


FIG. 12. (Color online) [(a) and (b)] X^- conditional probability plots for a hole fixed at $z/R=0$ and one of the electrons fixed at two different positions. (c) Both electrons are fixed. The highest probability of finding the remaining particle corresponds to the red areas. These plots were made for $R/a_{b,0}=20$, $\epsilon_1/\epsilon_0=10$, and $\sigma=5$.

is shown in Fig. 14 for $\sigma=0.53$ which is valid for thicker Si wires (for wires where the band gap is indirect, we take the mass of the electron at the X point, in this case we choose the lateral mass), and $\sigma=2.45$, valid for thin wires where the band gap becomes direct and we can use the mass of the electron at the Γ point (for this mass, the transverse mass at the X point would result in almost exactly the same curve due to the very small difference in σ). It is clear in Fig. 14 that the small difference in the value of σ results in small differences in the behavior as function of the wire radius. For the chosen parameters, the triplet state or excited state is always less bound than the singlet state or ground state. We found that the X^- and X^+ singlet binding energies could be, to a good approximation (within 1%), fitted to $-c/(R/a_{b,0})^d$. The values of the fitting parameters c and d for the singlet binding energies for several materials are given in Table II. We found that the triplet binding energies can be fitted to the same formula but, of course, with different parameters.

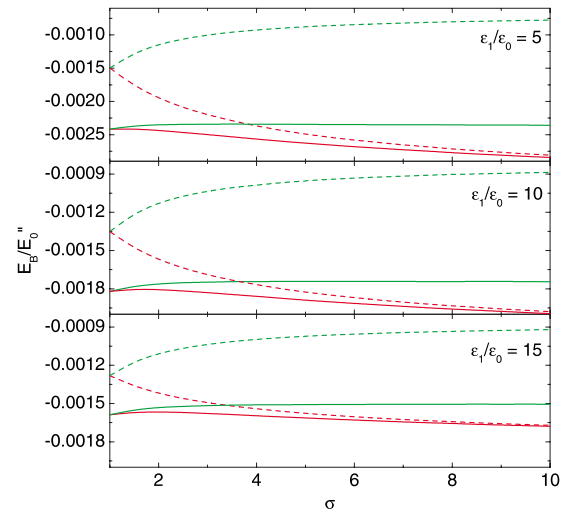


FIG. 13. (Color online) Singlet (full lines) and triplet (dashed lines) X^+ (red) and X^- (green) trion binding energies as function of $\sigma=m_h/m_e$ for $\epsilon_1/\epsilon_0=5, 10,$ and 15 and fixed $R/a_{b,0}=20$.

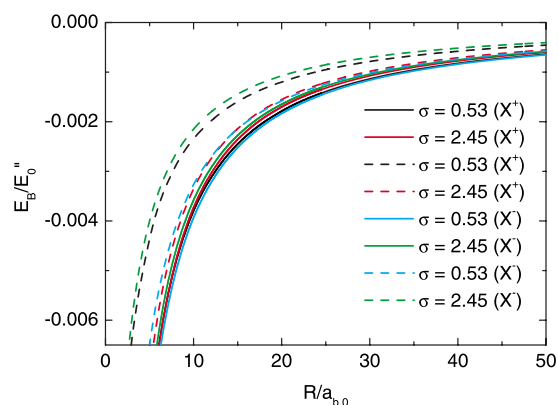


FIG. 14. (Color online) Trion singlet (full lines) and triplet (dashed lines) binding energies as function of the wire radius $R/a_{b,0}$ for $\epsilon_1/\epsilon_0=11.9$. We took $\sigma=0.53$ (Si at X) and $\sigma=2.45$ (Si at Γ).

V. CONCLUSION

In this paper, we studied the stability of positively and negatively charged excitons in wires with different dielectric constants. Due to our previous work on excitons, we were able to quickly and accurately reconstruct the effective 2D potential for trions, which enables calculations of trion binding energies on a 2D grid. We found that the negatively charged exciton has always a smaller binding energy than the positively charged exciton in a wire with $\sigma > 1$, even when the dielectric mismatch is larger. In the case of $\sigma < 1$, the opposite is true. This is in contrast to the embedded V-grooved wires²³ where it was found experimentally that for narrow widths $|E_B(X^-)| > |E_B(X^+)|$. Furthermore, we found that the dielectric mismatch does not change the quali-

TABLE II. Table with fitting parameters for the X^\pm singlet binding energy using the formula $-c/(R/a_{b,0})^d$.

	X^+		X^-	
	c	d	c	d
Si at X (t)	0.0465	1.100	0.0431	1.086
Si at X (l)	0.0422	1.052	0.0448	1.064
Si at Γ	0.0462	1.098	0.0430	1.085
InP	0.0520	1.126	0.0433	1.095
ZnO	0.0540	1.096	0.0485	1.079
Ge	0.0440	1.112	0.0397	1.093
GaAs	0.0501	1.120	0.0430	1.093
InAs	0.0536	1.144	0.0416	1.101

tative behavior of the σ dependence of the binding energy for the X^- trion, whereas the curves for the X^+ singlet state show a smaller σ dependence with increasing ϵ_1/ϵ_0 . We also studied the trion wave functions and discussed both correlation functions and conditional probabilities of the trions. These results show us the correlated arrangement of the particles in the wire. The binding energies as function of the wire radius exhibit, to a good approximation, a $1/R$ dependence.

ACKNOWLEDGMENTS

This work was supported by the UA-IMEC, vzw collaborative project, the Belgian Science Policy (IAP), the EU Network of Excellence, SANDiE, and BOF-TOP (University of Antwerp).

*an.slachmuylders@ua.ac.be

†bart.partoens@ua.ac.be

‡wim.magnus@imec.be

§francois.peeters@ua.ac.be

¹M. A. Lampert, Phys. Rev. Lett. **1**, 450 (1958).

²G. A. Thomas and T. M. Rice, Solid State Commun. **23**, 359 (1977).

³T. Kawabata, K. Muro, and S. Narita, Solid State Commun. **23**, 267 (1977).

⁴B. Stébé and A. Ainane, Superlattices Microstruct. **5**, 545 (1989).

⁵B. Szafran, B. Stébé, J. Adamowski, and S. Bednarek, Phys. Rev. B **66**, 165331 (2002).

⁶M. Law, J. Goldberger, and P. Yang, Annu. Rev. Mater. Res. **34**, 83 (2004).

⁷X. Duan, Y. Huang, Y. Cui, and C. M. Lieber, Nano Lett. **2**, 101 (2002).

⁸Y. Cui and C. M. Lieber, Science **291**, 851 (2001).

⁹X. Duan, Y. Huang, and C. M. Lieber, Nano Lett. **2**, 487 (2002).

¹⁰M. H. Huang, S. Mao, H. Feick, H. Yan, Y. Wu, E. Weber, R. Russo, and P. Yang, Science **292**, 1897 (2001).

¹¹X. Duan, Y. Huang, R. Agarwal, and C. M. Lieber, Nature (London) **421**, 241 (2003).

¹²B. Szafran, T. Chwiej, F. M. Peeters, S. Bednarek, and J. Ad-

amowski, Phys. Rev. B **71**, 235305 (2005).

¹³S. Baskoutas, Chem. Phys. Lett. **404**, 107 (2005).

¹⁴C. Riva, F. M. Peeters, and K. Varga, Phys. Rev. B **61**, 13873 (2000).

¹⁵A. S. Bracker, E. A. Stinaff, D. Gammon, M. E. Ware, J. G. Tischler, D. Park, D. Gershoni, A. V. Filinov, M. Bonitz, F. M. Peeters, and C. Riva, Phys. Rev. B **72**, 035332 (2005).

¹⁶A. F. Slachmuylders, B. Partoens, W. Magnus, and F. M. Peeters, Phys. Rev. B **74**, 235321 (2006).

¹⁷L. Bányai, I. Galbraith, C. Ell, and H. Haug, Phys. Rev. B **36**, 6099 (1987).

¹⁸A. F. Slachmuylders, B. Partoens, W. Magnus, and F. M. Peeters, J. Phys.: Condens. Matter **18**, 3951 (2006).

¹⁹I. Vurgaftman, J. R. Meyer, and L. R. Ram-Mohan, J. Appl. Phys. **89**, 5815 (2001).

²⁰G. Coli and K. K. Bajaj, Appl. Phys. Lett. **78**, 2861 (2001).

²¹<http://www.semiconductors.co.uk/>

²²A. J. Shields, M. Pepper, M. Y. Simmons, and D. A. Ritchie, Phys. Rev. B **52**, 7841 (1995).

²³T. Otterburg, D. Y. Oberli, M.-A. Dupertuis, N. Moret, E. Pelucchi, B. Dwir, K. Leifer, and E. Kapon, Phys. Rev. B **71**, 033301 (2005).